The Astrophysical Journal, 831:98 (12pp), 2016 November 1 doi:10.3847/0004-637X/831/1/98

GENERAL-RELATIVISTIC THREE-DIMENSIONAL MULTI-GROUP NEUTRINO RADIATION-HYDRODYNAMICS SIMULATIONS OF CORE-COLLAPSE SUPERNOVAE

Luke F. Roberts[1,9], Christian D. Ott[1,2], Roland Haas[1,3], Evan P. O'Connor[4,10], Peter Diener[5,6], and Erik Schnetter[5,7,8]
[1] TAPIR, Walter Burke Institute for Theoretical Physics, Mailcode 350-17, California Institute of Technology, Pasadena, CA 91125, USA; lroberts@tapir.caltech.edu
[2] Yukawa Institute for Theoretical Physics, Kyoto University, Kyoto, Japan
[3] Max Planck Institut für Gravitationsphysik, Potsdam, Germany
[4] Department of Physics and Astronomy, North Carolina State University, NC, USA
[5] Center for Computation & Technology, Louisiana State University, Baton Rouge, USA
[6] Department of Physics & Astronomy, Louisiana State University, Baton Rouge, USA
[7] Perimeter Institute for Theoretical Physics, Waterloo, ON, Canada
[8] Department of Physics, University of Guelph, Guelph, ON, Canada
Received 2016 April 26; revised 2016 July 26; accepted 2016 July 26; published 2016 October 28

ABSTRACT

We report on a set of long-term general-relativistic three-dimensional (3D) multi-group (energy-dependent) neutrino radiation-hydrodynamics simulations of core-collapse supernovae. We employ a full 3D two-moment scheme with the local M1 closure, three neutrino species, and 12 energy groups per species. With this, we follow the post-core-bounce evolution of the core of a nonrotating 27-$M_\odot$ progenitor in full unconstrained 3D and in octant symmetry for $\gtrsim$380 ms. We find the development of an asymmetric runaway explosion in our unconstrained simulation. We test the resolution dependence of our results and, in agreement with previous work, find that low resolution artificially aids explosion and leads to an earlier runaway expansion of the shock. At low resolution, the octant and full 3D dynamics are qualitatively very similar, but at high resolution, only the full 3D simulation exhibits the onset of explosion.

Key words: instabilities – neutrinos – supernovae: general

1. INTRODUCTION

Although it has been studied for many decades, the mechanism driving core-collapse supernova explosions (CCSNe) is still uncertain and remains an area of active research (e.g., Janka 2012; Burrows 2013). The delayed neutrino mechanism (Bethe & Wilson 1985), in combination with multi-dimensional fluid instabilities, seems to be the most promising mechanism driving garden-variety CCSNe. However, it cannot deliver the explosion energies seen in some extreme CCSNe (hypernovae). Another mechanism is most likely to be at work in these events, possibly relying on rotation and magnetic fields (e.g., Burrows et al. 2007; Mösta et al. 2014b, 2015).

The hydrodynamic shock formed at core bounce stalls due to energy loss to the dissociation of heavy nuclei and to neutrinos. The delayed neutrino-heating model for CCSNe posits that a small fraction of the neutrinos emitted from near the protoneutron star are absorbed near the stalled shock, thereby depositing enough energy to reinvigorate the shock's outward progress. This shock revival must occur within a few hundreds of milliseconds to ~1–2 s of core bounce to avoid black hole formation or a top-heavy neutron star mass distribution (O'Connor & Ott 2011). Since the neutrino mechanism strongly depends on how efficiently energy is transported by neutrinos from near the protoneutron star to the region just behind the shock and on how this energy deposition affects the hydrodynamic evolution near the shock, an accurate treatment of hydrodynamics and non-equilibrium neutrino transport is a key requirement for simulating CCSNe.

Imposing symmetries on simulations of CCSNe can have significant consequences for their evolution (e.g., Hanke et al. 2012; Couch 2013; Murphy et al. 2013). Detailed spherically symmetric one-dimensional (1D) simulations do not explode (Liebendörfer et al. 2001), except when particular low-mass progenitor models are used (e.g., Fischer et al. 2010; Hüdepohl et al. 2010). Multiple simulations including energy-dependent (multi-group) neutrino transport and imposing axial symmetry (2D) do exhibit explosions (Müller et al. 2012b, 2012a; Bruenn et al. 2013, 2016), although some do not (Dolence et al. 2015). Interestingly, the first simulations including ray-by-ray neutrino transport[11] without symmetries imposed three-dimensionally on the hydrodynamics did not find explosions in models that exploded when axisymmetry was assumed (Hanke et al. 2013). Melson et al. (2015) showed that in three-dimensional (3D) simulations that are close to the threshold of explosion, modified neutrino interaction physics can facilitate explosion. Lentz et al. (2015) carried out 1D, two-dimensional 2D, and 3D simulations using a ray-by-ray multi-group flux-limited diffusion approximation to neutrino transport. They found explosions in 2D and 3D, with an earlier onset of explosion in 2D.

The differences between 2D and 3D are likely due to the evolution of postshock hydrodynamic instabilities—namely, standing accretion shock instability (SASI) and turbulent convection—when different symmetries are enforced (Couch 2013; Couch & Ott 2015). Clearly, these non-radial instabilities are completely suppressed in spherical symmetry. There are also significant differences between 2D and full 3D for both of these instabilities. Azimuthal modes are suppressed in axisymmetry, which has consequences for the evolution of SASI (e.g., Iwakami et al. 2008). Additionally, it is well known that the properties of two-dimensional turbulence differ

[9] NASA Einstein Fellow.
[10] NASA Hubble Fellow.
[11] Ray-by-ray solves individual 1D transport problems along radial rays that are coupled via lateral advection terms.

significantly from those of 3D turbulence (Kraichnan 1967; Hanke et al. 2012). In particular, 2D turbulence, because of the conservation of enstrophy in 2D, exhibits an inverse cascade. This inverse cascade transfers kinetic energy to large scales, where it can artificially aid explosion (Couch & O'Connor 2014; Couch & Ott 2015).

An accurate treatment of neutrino transport is crucial to simulating CCSNe. The neutrino mechanism hinges on how efficiently neutrinos can move energy from where they decouple from the fluid near the protoneutron star to just behind the shock (e.g., Janka 2012). It appears that the success or failure of 3D CCSN simulations is sensitive to the detailed properties of the neutrino field. In parameterized studies, increasing the neutrino heating by just ~5% can cause models to go from failure to explosion (Ott et al. 2013). In models with more realistic neutrino transport, small variations in the neutrino opacities can mean the difference between success and failure (Melson et al. 2015). Because of the strong energy dependence of weak processes and the non-equilibrium nature of the neutrino field, CCSN simulations require evolving the energy, and angle-dependent neutrino distribution functions. In 3D time-dependent CCSN simulations, solving the full Boltzmann equation is still computationally prohibitive (but see Sumiyoshi et al. 2015 for static Boltzmann solutions). To date, 3D radiation-hydrodynamics simulations of CCSNe have employed spectral, one-moment or two-moment radiation transport schemes in the ray-by-ray approximation (e.g., Lentz et al. 2015; Melson et al. 2015). Some argue that this approximation may overestimate spatial variations in the neutrino field (e.g., Sumiyoshi et al. 2015; Skinner et al. 2015).

General-relativistic (GR) gravity is another important ingredient in CCSN simulations. Compared to simulations in Newtonian gravity, GR simulations result in more compact protoneutron stars from which neutrinos decouple at smaller radii and higher temperatures, resulting in harder spectra. This effect appears to outweigh the gravitational redshift and leads to a higher neutrino heating efficiency. Müller et al. (2012b) compared Newtonian, approximate GR, and conformally flat GR (exact in spherical symmetry) simulations in 2D for a 15-$M_\odot$ progenitor and found an explosion only in the GR case. O'Connor & Couch (2015) compared 2D Newtonian and approximate GR simulations and also found GR effects to be essential for explosions.

In this paper, we present long-term, fully 3D radiation-hydrodynamics simulations of the postbounce phase of CCSNe. Both hydrodynamics and neutrino radiation are evolved and coupled on the same 3D grid. Our simulations are performed with the `Zelmani` core-collapse simulation package (Ott et al. 2012, 2013; Reisswig et al. 2013), which includes GR hydrodynamics and GR spacetime evolution. For the first time, we use a new 3D implementation of the GR spectral two-moment M1 approximation to neutrino transport introduced by Shibata et al. (2011).

We carry out radiation-hydrodynamics simulations of the postbounce evolution of a 27 $M_\odot$ progenitor star in full 3D and, for comparison, in octant symmetry, restricting the flow to an octant of the 3D cube. All simulations are run to $\gtrsim$380 ms after core bounce, and each simulation is carried out at two resolutions to test the dependence of the outcome on the numerical resolution.

We find that the shock in the full 3D model begins to run away at around 220 ms after bounce in our highest-resolution run, suggesting that this model will achieve an explosion. A model run at half this resolution experiences shock runaway at around the same time, but shock expansion is much more rapid. Imposing octant symmetry on the high-resolution run prevents shock runaway. In the lower-resolution simulation, octant symmetry does not prevent shock runaway but does marginally reduce the shock expansion rate relative to the full simulation.

The remainder of this paper is structured as follows. In Section 2, we describe our simulation approach, setup, and inputs. We discuss our simulation results in Sections 3 and 4 and conclude in Section 5.

2. METHODS AND SETUP

We employ the GR `Zelmani` CCSN simulation package described in Ott et al. (2012, 2013) and Reisswig et al. (2013). `Zelmani` is based on the open-source `Einstein Toolkit` (Löffler et al. 2012; Mösta et al. 2014a) and implements GR hydrodynamics and spacetime evolution with adaptive mesh refinement (AMR). See Ott et al. (2013), Reisswig et al. (2013), and Löffler et al. (2012) for implementation details.

Within `Zelmani`, we have developed a multi-energy group GR M1 transport solver that evolves the radiation energy density E_ν and the radiation momentum density F_ν^i in the observer frame via the conservation equations

$$\partial_t \bar{E} + \partial_j(\alpha \bar{F}^j - \beta^j \bar{E}) + \partial_\nu(\nu\alpha n_\alpha \bar{M}^{\alpha\beta\lambda} n_{\lambda;\beta}) = \alpha[\bar{P}^{ij}K_{ij} - \bar{F}^j \partial_j \ln\alpha - \bar{S}^\alpha n_\alpha], \quad (1)$$

and

$$\partial_t \bar{F}_i + \partial_j(\alpha \bar{P}_i^j - \beta^j \bar{F}_i) - \partial_\nu(\nu\alpha\gamma_{i\alpha}\bar{M}^{\alpha\beta\lambda} n_{\lambda;\beta}) = \bar{F}_k \partial_i \beta^k - \bar{E}\partial_i\alpha + \alpha\frac{\bar{P}^{jk}}{2}\partial_i\gamma_{jk} + \alpha\bar{S}^\alpha\gamma_{i\alpha}, \quad (2)$$

where in the standard 3 + 1 GR notation, α is the lapse, β_i is the shift, γ_{ij} is the three-metric, K_{ij} is the extrinsic curvature, n^α is the four-velocity of the laboratory frame, $M^{\alpha\beta\lambda}$ is the third-order radiation moment (see Thorne 1981), S^α is the neutrino source term, and P^{ij} is the radiation momentum tensor. Overbars denote densitized quantities—for example, $\bar{E} = \sqrt{\det(\gamma_{ij})}E$. To close this system of equations, we assume $P^{ij} = P^{ij}(E_\nu, F_\nu^i)$ by interpolating between the optically thin and optically thick limits given in Shibata et al. (2011). We employ the Minerbo closure to interpolate between the optically thick and thin limits of the radiation pressure tensor and third-order radiation moment in the fluid rest frame (Minerbo 1978). This is similar to the approaches discussed in Shibata et al. (2011) and Cardall et al. (2013) and used in Just et al. (2015), O'Connor & Couch (2015), and Kuroda et al. (2016). Our numerical scheme is very similar to the gray scheme described in Foucart et al. (2015). The conservative moment equations shown above are evolved using a finite-volume scheme, where the radiation quantities are reconstructed at zone edges using the minmod limiter and we solve the resulting Riemann problems approximately using the HLLE solver. The source terms are treated in a locally implicit fashion, while the red shifting terms are treated using an explicit finite-volume upwind scheme. We evolve the velocity *independent* radiation transport equations because we find numerical instabilities in the high optical depth limit when

velocity dependence is included. Given that velocities behind shock in the postbounce phase are small compared to the speed of light, this should be a reasonable approximation. We do not explicitly enforce lepton number conservation.

We draw from Woosley et al. (2002) the progenitor model s27, which has been studied in a number of previous works (e.g., Müller et al. 2012a; Hanke et al. 2013; Ott et al. 2013; Couch & O'Connor 2014; Abdikamalov et al. 2015). In all simulations, we employ the $K_0 = 220$ MeV variant of the equation of state of Lattimer & Swesty (1991) in the form described in O'Connor & Ott (2010). We follow collapse and the very early postbounce phase in 1D using the open-source `GR1D` code (O'Connor & Ott 2013; O'Connor 2015) without explicit velocity dependence and the subset of Bruenn (1985) neutrino opacities laid out in O'Connor & Ott (2013), implemented via `NuLib` (O'Connor 2015). We use identical `NuLib` opacity tables in `GR1D` and `Zelmani`, consider three neutrino species (ν_e, $\bar{\nu}_e$, and $\nu_x = [\nu_\mu, \bar{\nu}_\mu, \nu_\tau, \bar{\nu}_\tau]$), and 12 energy groups, spaced logarithmically with bin-center energies between 1 MeV and 248 MeV.

We map to `Zelmani` at 30 ms after bounce and continue the simulations in 3D with identical microphysics. For mapping, we convert the `GR1D` metric to isotropic coordinates and resolve the Hamiltonian constraint in 1D (e.g., Baumgarte & Shapiro 2010). The neutrino fields are initialized to be in equilibrium with the background fluid, which results in a short initial transient in the luminosities and average neutrino energies.

We carry out simulations in full 3D ("s27FH") without any symmetry constraints and constrained "octant" 3D simulations ("s27OH"), in which we simulate only in an octant of the 3D cube with reflective boundaries on the $x-z$, $x-y$, and $y-z$ planes. Additionally, we carry out lower-resolution simulations in full 3D and octant 3D, which we denote as "s27FL" and "s27OL," respectively. Note that our octant simulations differ from the rotational octant symmetry employed, e.g., in Ott et al. (2012), where periodic boundary conditions are enforced on the $x-z$ and $y-z$ planes. This prevents us from following any net rotation and likely changes the character of flows near the boundaries. This choice is made not for physical reasons, but for computational savings.

All 3D simulations use Cartesian AMR with eight levels of refinement. We do not employ the multiblock setup of Reisswig et al. (2013). Each level increases the resolution by a factor of two. The coarsest level extends to ∼6140 km. We carry out simulations at two resolutions. In the s27FH and s27OH simulations, the finest grid covering the protoneutron star has a linear cell size of $\Delta x = 370$ m, and we use AMR to keep the entire postshock region covered by the third-finest grid with $\Delta x = 1.48$ km (corresponding to an angular resolution of $\sim 0\overset{\circ}{.}85$ at a radius of 100 km). In the s27FL, the finest linear cell size is the same as in the high-resolution simulation, but we cover the postshock region with the fourth-finest grid with $\Delta x = 2.96$ km (corresponding to an angular resolution of $\sim 1\overset{\circ}{.}7$ at a radius of 100 km). In s27OL, the cell size on every refinement level is doubled relative to the "high-resolution" simulations, and the shock is followed on the third-finest grid with $\Delta x = 2.96$ km.

3. RESULTS

We follow all four models for $\gtrsim$380 ms after core bounce or until the supernova (SN) shock has clearly run away. Figure 1 depicts entropy colormaps of equatorial slices of all models at selected times. At late times, differences in the numerical resolution and imposed symmetries can result in qualitatively different evolution. Both s27FL and s27OL have experienced shock runaway by ∼280 ms and have expanding high-entropy regions and low-entropy accretion streams similar to what are seen in the simulations of Lentz et al. (2015) and Melson et al. (2015), although these other simulations employed different progenitors and had very different hydrodynamic evolutions. In contrast, the s27OH shock has begun to contract by 300 ms and does not contain large-scale, coherent low-entropy downflows or high-entropy outflows. The high-resolution, full 3D simulation s27FH has a continuously growing and deformed postshock region, but does not run away as quickly as its low-resolution counterparts. Once again, the coherent low-entropy accretion streams are less prominent than the ones found in s27FL. The evolutions of angle-averaged thermodynamic quantities in the postshock region of s27FH are shown in Figure 2. The shaded regions in this figure indicate angular variations that steadily grow with increasing postbounce time.

Our simulations are too computationally expensive to continue once the SN shock expands to large radii beyond ∼500 km, since we use AMR to keep the entire postshock region at constant resolution.[12] Therefore, we cannot follow the evolution long enough to predict reliable explosion energies (or the diagnostic energies considered in, e.g., Lentz et al. 2015). Rapid shock expansion is our best indicator of a possible explosion. In Figure 3, we present the angle-averaged shock radius along with the angular variation of the shock's position, indicated by shaded areas, bounded by the minimum and maximum shock radii. In all models, there are initially small oscillations as the model relaxes after mapping from `GR1D`'s 1D spherical grid to `Zelmani`'s 3D Cartesian AMR grid. Then the shock expands slowly and secularly over the first ∼120 ms. The shock settles at ∼150–180 km. In the high-resolution models, the shock recedes slightly, and the differences between s27FH and s27OH simulations are very modest at this time. In the low-resolution models, again independent of full/octant 3D, the shock maintains a nearly constant average radius for ∼80–100 ms. The deviation of the minimum and maximum shock radii from the average radius begins to increase over this period as the gain region starts to convect in all simulations. Around 230 ms after bounce, the average shock radius begins to expand once again for all models. The silicon–oxygen shell interface of the progenitor crosses the SN shock at this time, and the accretion rate drops significantly (see Figure 3). This is in agreement with the 3D simulation of Hanke et al. (2013) (see their Figure 2); however, they did not find an explosion in 3D. In fact, the evolution of the shock in our model s27OH is quite similar to the shock radius evolution seen in Hanke et al. (2013).

Clearly, the evolution of the shock depends significantly on both the resolution of the simulation and on whether or not symmetries are imposed. As some of us found in the parameterized 3D simulations of Abdikamalov et al. (2015), lower resolution appears to be more favorable for shock runaway for simulations near the threshold of explosion (cf. Radice et al. 2016). At low resolution, imposing octant symmetry does not have a large effect on the dynamics in

[12] When we stop it, the s27FH simulation requires about 15 TB of main memory and is running on 19,200 NSF/NCSA Blue Waters CPU cores. The computational cost of this model is approximately 60 million CPU hours.

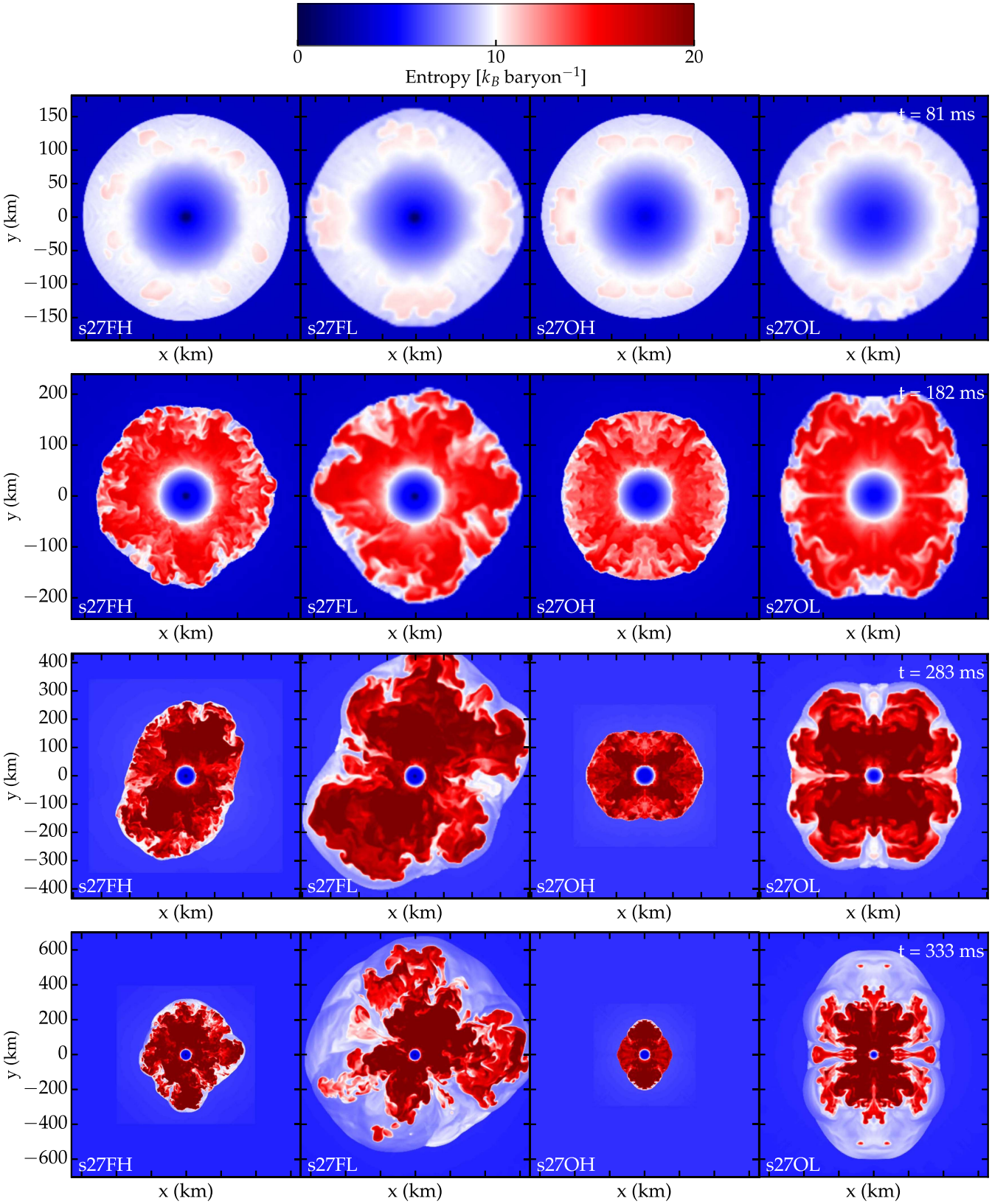

Figure 1. Cross-sections of the entropy distribution at selected times. The left panels show the model s27FH, the second from left panels show s27FL, the second from right panels show s27OH, and the right panels show s27OL. The *x*-axis has the same scale as the *y*-axis. Notice that the spatial scale changes in different rows, but the entropy colormap stays constant. The slight jump in coloration in the accretion flow is artificial. We plot only the refinement level that includes the shock, and outside of this region we choose a constant background color to approximately match the coloration of the accretion flow.

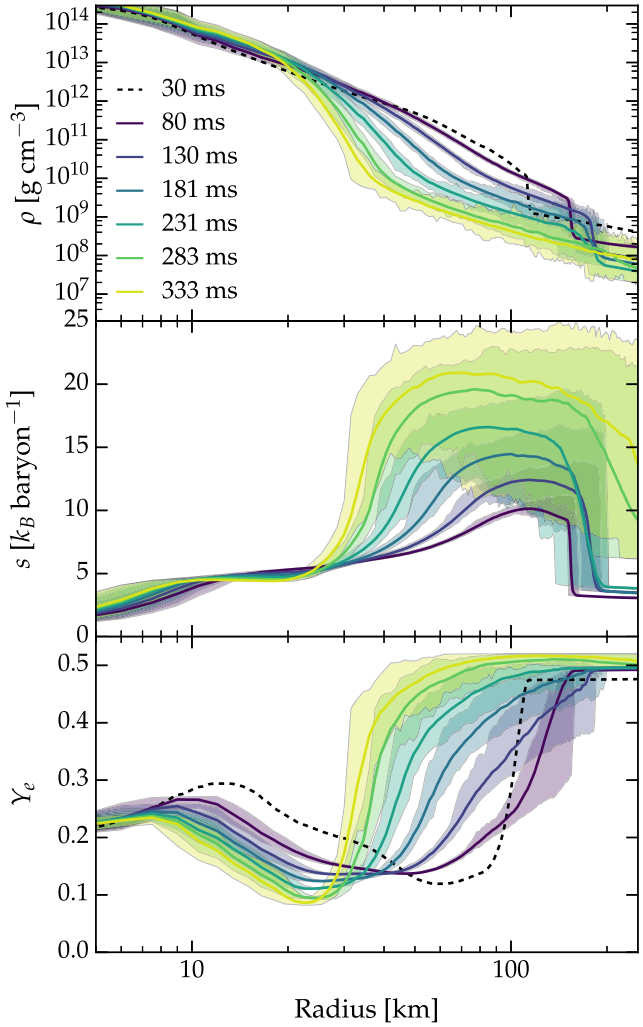

Figure 2. Evolution of the thermodynamic state of the gain region of s27FH. The solid lines show the angle-averaged density, entropy, and electron fraction of the ejecta, while the shaded regions show the minimum and maximum of these quantities on spherical shells. The dashed lines show the initial conditions of our 3D simulations.

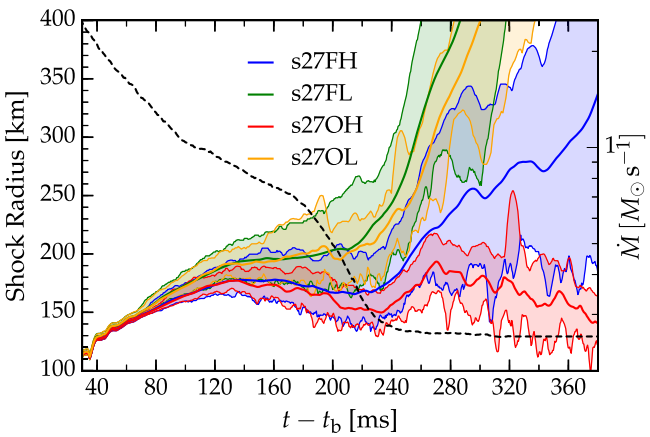

Figure 3. Evolution of the supernova shock. The thick lines show the angular average of the shock radius for all four models considered in this work. For all four models, the shaded regions show the minimum and maximum radii of the shock at a given time. The dashed line shows the mass accretion rate in s27OL just outside the shock. The accretion rates for the other three models are similar.

the gain region. Both s27FL and s27OL run away very quickly after the mass accretion rate falls off, with s27OL lagging by only a few milliseconds. The high-resolution full 3D simulation s27FH runs away more slowly than the low-resolution simulations, but it nonetheless is headed toward explosion, reaching a maximum shock radius of more than 400 km and an average shock radius of ∼315 km at 370 ms after core bounce. The minimum shock radius of s27FH barely expands after 260 ms, which is quite different from what is seen in the low-resolution models that experience rapid runaway in all directions. In the octant high-resolution simulation s27OH, the shock begins to once again recede soon after the passage of the silicon–oxygen shell interface. It seems very likely that s27OH will result in a failed SN, the two low-resolution models are very likely to explode, and s27FH seems to be clearly on the path to explosion.

In Figure 5, we show the decomposition of the shock front into real spherical harmonic modes following the convention in Burrows et al. (2012), except that our spherical harmonic coefficients $a_{\ell,m}$ are larger by a factor of $\sqrt{2\ell+1}$. We present the root-mean-square amplitudes $A_\ell = \sqrt{\sum_m a_{\ell m}^2}$ (where $a_{\ell,m}$ is a coefficient of the spherical harmonic decomposition of $R_{\rm shock}(\theta, \phi)$). The top two panels show the evolutions of the $\ell = 1$ (for full 3D simulations) and $\ell = 2$ shock modes (for all models). For the high-resolution full-3D model s27FH, we show $\ell = 1$ to $\ell = 5$ in the bottom panel. Considering an expansion in a real spherical harmonic basis, our reflecting octant symmetry suppresses odd ℓ modes, all negative azimuthal modes, and odd azimuthal modes so that only the $\{\ell = 0, 2, \ldots; m = 0, 2, 4, \ldots, \ell\}$ modes can be excited. This is in contrast to rotating octant symmetry, which allows for the modes $\{\ell = 0, 2, \ldots; m = 0, \pm 4, \pm 8, \pm \ell\}$. This is very different from axial symmetry (i.e., 2D simulations), where all of the ℓ modes can exist but all m modes except $m = 0$ are suppressed and small-scale motions are effectively constrained to two dimensions.

All of the models experience increasing deviations from spherical symmetry with increasing postbounce time. Although the asymmetry grows with time, none of the models appear to be dominated by SASI (Blondin et al. 2003). There is a period in s27FH from ∼120 ms to ∼240 ms where the $\ell = 1$ mode oscillates with constant frequency and grows, which may be indicative of SASI activity. Nevertheless, these coherent oscillations are destroyed once the Si shell interface is accreted through the shock. Additionally, higher ℓ modes seem to grow at the same rate. It is possible that the growth of low-order asymmetries without coherent oscillation is due to SASI (which predicts longer-period oscillations with increased neutrino heating; Yamasaki & Yamada 2007; Scheck et al. 2008), but it appears more likely that this asymmetry is driven by convective instability in the postshock region (see Figure 4). SASI has been observed in some models that use the same s27 progenitor model and hydrodynamics code but include only parameterized neutrino physics (Ott et al. 2013; Abdikamalov et al. 2015). Strong SASI activity occurred in these models only when the parameterized neutrino heating rate was low and shock runaway did not occur. When the parameterized neutrino heating rate was higher, neutrino-driven convection dominated, and much longer period (∼20 ms) quasi-oscillatory behavior was observed, similar to what we find here.

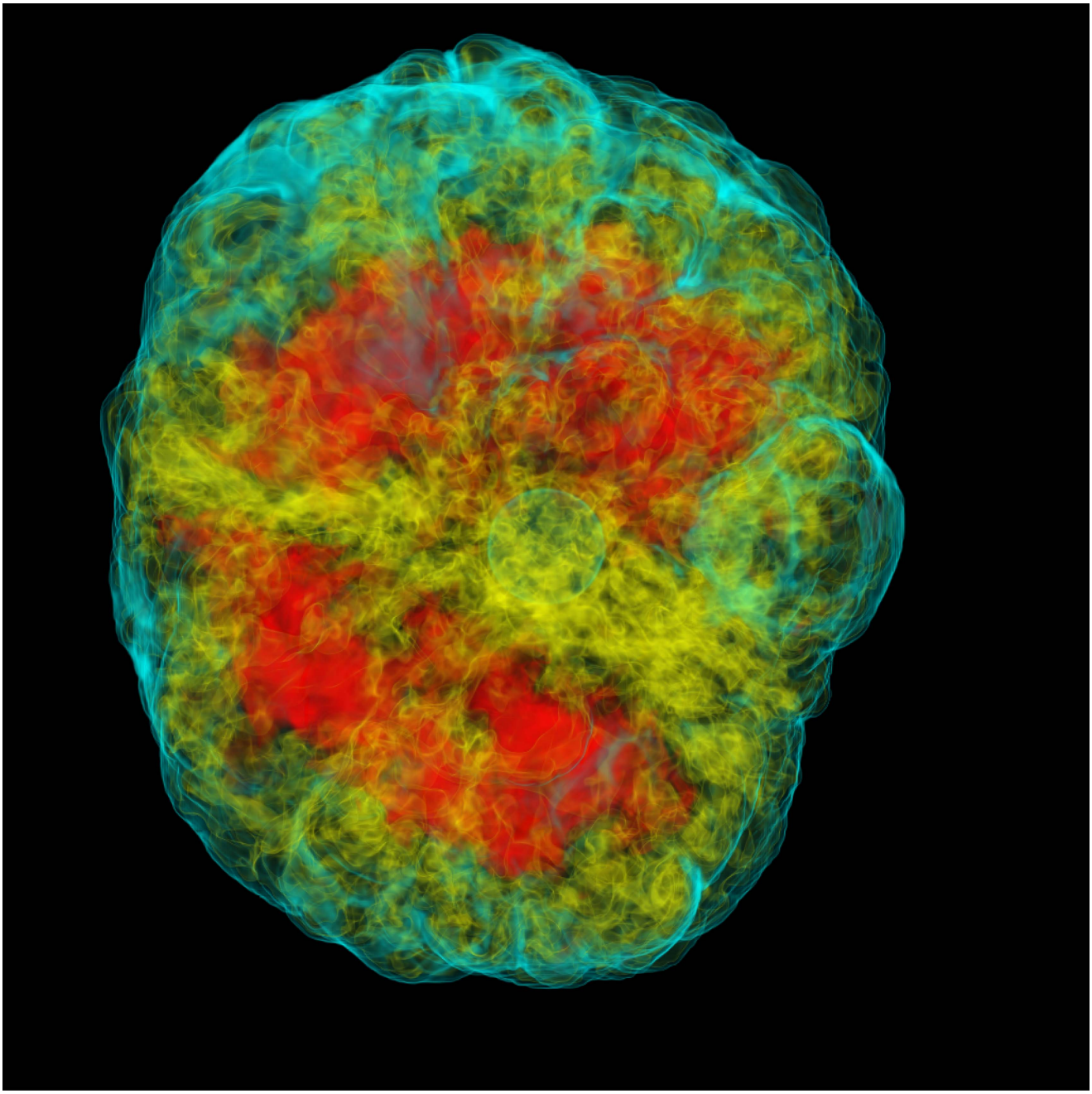

Figure 4. Volume rendering of the entropy distribution in the full 3D unconstrained high-resolution simulation s27FH at 283 ms after core bounce. The cyan surface corresponds to the shock front and is at a specific entropy of 10 k_B baryon^{-1}. The yellow regions are at specific entropies of $\sim$16 k_B baryon^{-1}, and the red regions are at $\sim$20 k_B baryon^{-1}. They correspond to strongly neutrino-heated bubbles of hot gas that expand, pushing the shock outward locally and globally. This results in a complicated shock morphology that is asymmetric on a large scale and on a small scale. This figure was produced using `yt` (Turk et al. 2011).

In the two unconstrained full 3D simulations, the $\ell = 1$ mode begins to grow rapidly once shock runaway occurs. Comparing this with Figure 1, we see that the late-time asymmetry is driven by large solid angle regions of high-entropy outflow and cold accretion streams that penetrate to near the protoneutron star. Both $\ell = 1$ and $\ell = 2$ asymmetry increase during the late shock expansion period of s27FH, although it appears that the $\ell = 1$ deformation is running away more rapidly. While it is not completely clear that the shock is running away in s27FH, this increasingly asymmetric expansion is similar to what is seen in s27FL, which clearly experiences shock runaway. There is also strong $\ell = 2$ deformation in s27OL after runaway. Although s27OH does not experience shock runaway, it shows continued growth of the $\ell = 2$ and exhibits violent oscillations in the magnitude of the shock deformation. This may indicate that $\ell = 2$ SASI is occurring in this model, although the flow is not well ordered and it is hard to unambiguously determine the contribution of convection relative to the SASI.

In Figure 6, we show the spherically averaged properties of the neutrino field at a radius of 450 km for all four models. Initially, there is a short period of oscillation in all quantities as the initial spherically symmetric model relaxes on our 3D Cartesian grid. These oscillations cease by $\sim$40 ms after

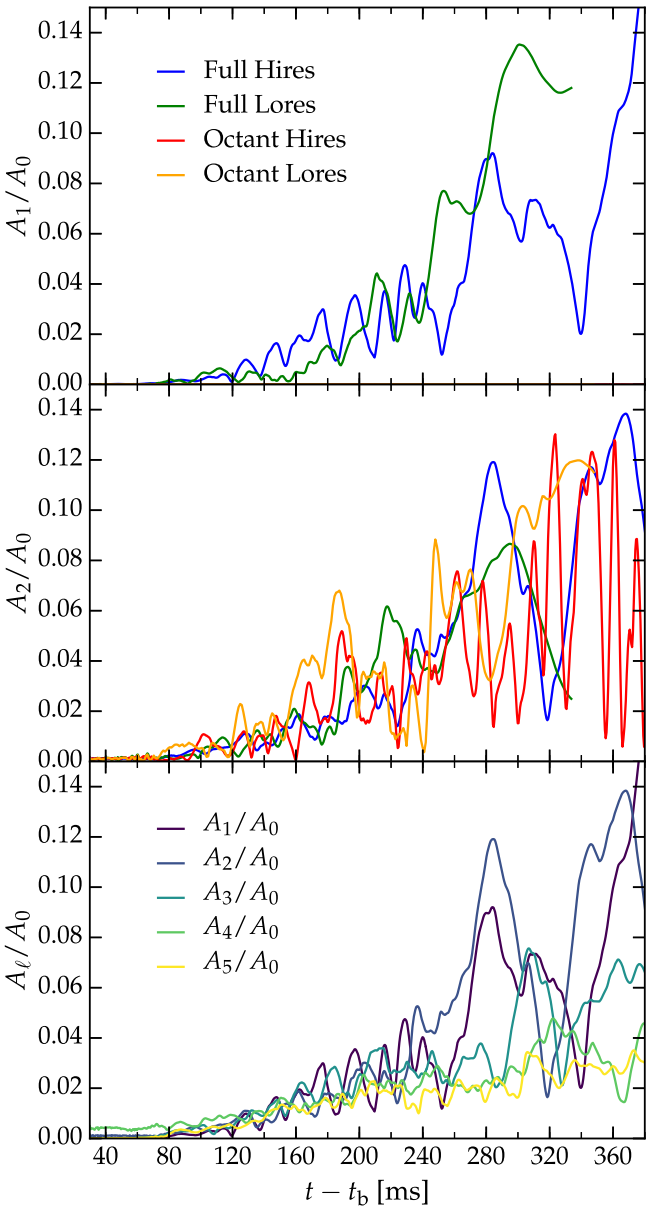

Figure 5. Evolution of the real spherical harmonic deformation of the supernova shock front. Top Panel: the rms m modes of the $\ell = 1$ spherical harmonic normalized to the $\ell = 0$, $m = 0$ mode. Octant symmetry forces all $\ell = 0$ modes to be zero. Middle Panel: similar to the top panel, except for the $\ell = 2$ mode. Bottom Panel: evolution of the first five ℓ-modes of s27FH.

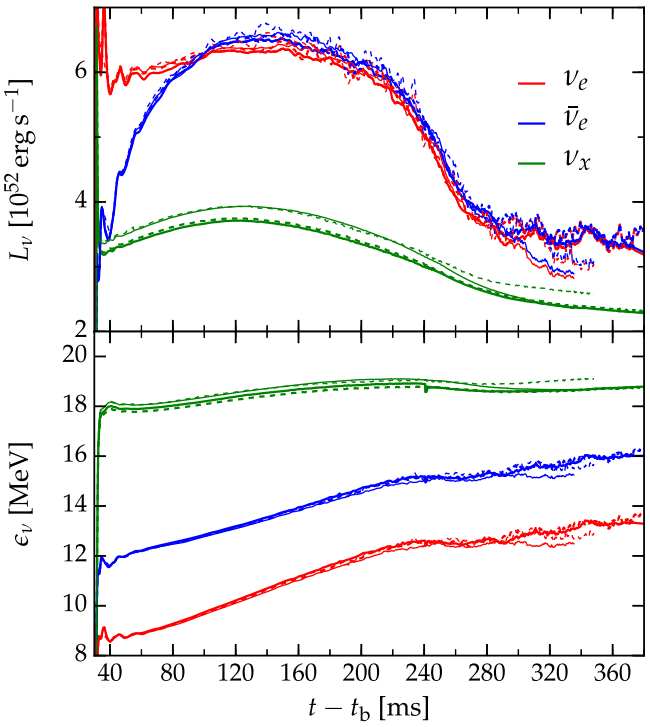

Figure 6. Spherically averaged properties of the neutrino field at a radius of 450 km for the models s27FH (thick solid lines), s27FL (thin solid lines), s27OH (thick dashed lines), and s27OL (thin dashed lines). The top panel shows the ν_e (red lines), $\bar{\nu}_e$ (blue lines), and ν_x (green lines) luminosities as functions of time. The luminosities of s27OH are indistinguishable from those of the model s27FH for the first 280 ms. The lower panel shows the mean neutrino energies as a function of time.

bounce, and then the spatially averaged neutrino evolution is smooth. Until ∼280 ms after bounce, there are only small differences between the neutrino luminosities in all models. Deviations after this time are due to large variations in the extent and geometry of the postshock region and changes in the accretion rate through the gain region (cf. Figures 1 and 3).

All four models exhibit very similar average neutrino energies, the expected hierarchy of neutrino energies, $\langle\epsilon_{\nu_e}\rangle < \langle\epsilon_{\bar{\nu}_e}\rangle < \langle\epsilon_{\nu_{\mu/\tau}}\rangle$, and spectral hardening as a function of time. The high average energies of $\nu_{\mu/\tau}$, relative to the average energies predicted by other groups (e.g., Müller & Janka 2014), are due to our neglect of inelastic neutrino scattering. This is unlikely to have a strong effect on heating in the gain region, since μ and τ neutrinos do not effectively deposit their energy there. Müller et al. (2012b) have shown that the inelastic scattering of heavy-flavored neutrinos near the electron antineutrino sphere can modestly increase the average energies and luminosity of electron-flavored antineutrinos (by at most 10%). Therefore, the neglect of inelastic scattering in our models may change our quantitative results but is unlikely to make a qualitative difference in the outcome of our simulations. The slight offset in the ν_x luminosities between the low- and high-resolution runs is due to the different resolutions near their neutrinospheres. Tamborra et al. (2014b) have also investigated 3D models of CCSNe using the s27 progenitor. Our ν_e and $\bar{\nu}_e$ luminosities and average energies are within 10% of those found by Tamborra et al. (2014b), but our simulations show a different hierarchy of luminosities from theirs, with $L_{\nu_e} < L_{\bar{\nu}_e}$. Our $\nu_{\mu/\tau}$ luminosities are also about 25% lower than those reported in Tamborra et al. (2014b).

Additionally, Tamborra et al. (2014) found that the lepton flux is asymmetric about the center of mass with a strong dipole component, i.e., their models exhibit lepton emission self-sustained asymmetry (LESA). In model s27FH, we find that the dipole moment of the lepton flux is less than 10% of the monopole term at 280 ms after bounce. Before and after that time, it is even smaller. Therefore, we do not see strong evidence for LESA in our highest-resolution model. Conversely, Tamborra et al. (2014) found a dipole moment of the same order as the monopole moment at 280 ms after bounce when using the same progenitor model.

There are a number of possible reasons for this discrepancy. First, it has been suggested that the formation of LESA is related to protoneutron star convection (Tamborra et al. 2014). In s27FH, we see protoneutron star convection begin to

develop only ∼230 ms after bounce, and it becomes fully developed only by ∼280 ms. The late onset of protoneutron star convection is possibly due to the entropy and lepton number gradients in our initial postbounce model, which does not include velocity dependence and inelastic neutrino scattering during collapse. The neglect of these effects can significantly impact the gradients of entropy and lepton number inside the gain radius (Lentz et al. 2012). Additionally, we employ a set of neutrino opacities that differ in detail from the opacities used by Tamborra et al. (2014), which can result in a different evolution of entropy and lepton number gradients. It is also possible that the full 3D neutrino transport we employ, as opposed to the "ray-by-ray" approximation used by Tamborra et al. (2014), washes out asymmetries in the neutrino field that drive LESA (Skinner et al. 2015; Sumiyoshi et al. 2015). We emphasize that there are many other differences between our neutrino transport scheme and the scheme used by Tamborra et al. (2014), so the absence of LESA in our models cannot be unequivocally attributed to the difference between full 3D transport and the "ray-by-ray" approximation.

4. DISCUSSION

In view of the small variations in neutrino properties between models, the results of the previous section suggest that the effect of resolution and symmetries on the postshock hydrodynamics and, consequently, on the shock radius evolution is of paramount importance. The large variation of shock evolution with resolution suggests that the postshock hydrodynamics in our models are unconverged (Radice et al. 2016). Although our highest-resolution simulation is the highest-resolution unconstrained neutrino radiation-hydrodynamics simulation performed to date, it is still likely to be severely underresolved. In Abdikamalov et al. (2015), the effective Reynolds number due to numerical viscosity in simulations at the resolution employed here was estimated to be around 70. This is many orders of magnitude lower than the physical Reynolds number in these systems (although there is no one-to-one correspondence between physical and numerical viscosity; Radice et al. 2015). Clearly, convectively driven turbulence will behave differently at this low Reynolds number relative to what would happen at the physical Reynolds number (Abdikamalov et al. 2015; Radice et al. 2016). Abdikamalov et al. (2015) suggested that altering the resolution changes the numerical viscosity and alters the spectrum of turbulence. It is also possible that coarser Cartesian grids provide larger perturbations from which turbulent convection can grow (Ott et al. 2013). The size of the initial perturbations is important since they must grow to macroscopic scales and become buoyant before being advected out of the convectively unstable region (Foglizzo et al. 2006; Scheck et al. 2008).

The difference between unconstrained simulations and simulations enforcing cylindrical symmetry has also been studied extensively, both with parameterized or simplified neutrino physics (Nordhaus et al. 2010; Hanke et al. 2012; Couch 2013; Dolence et al. 2013; Couch & O'Connor 2014; Handy et al. 2014) and in models employing realistic neutrino transport (Lentz et al. 2015). The combined result of these previous works has been somewhat inconclusive, but on the whole they seem to (artificially) favor explosions in axisymmetry over full 3D. Axisymmetry suppresses $m \neq 0$ large-scale modes and makes a fluid behave as it would in two dimensions at small scales. Both of these effects are likely to be important,

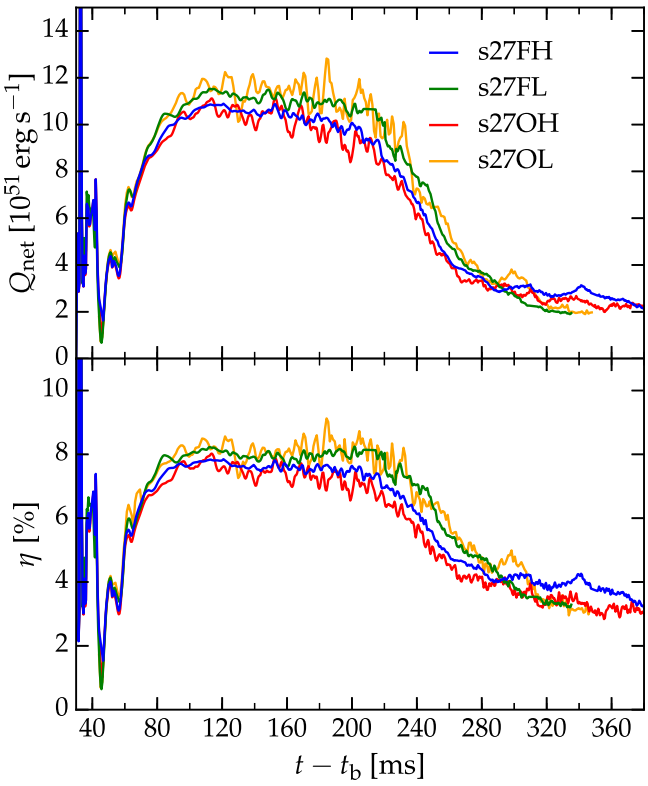

Figure 7. Top panel: the net neutrino heating rate in the gain region as a function of time for s27FH (blue), s27OH (red), s27FL (green), and s27OL (orange) averaged over a window of 2.5 ms. Bottom Panel: heating efficiency, $\eta = Q_{\rm net}/(L_{\nu_e} + L_{\bar{\nu}_e})$, for these models.

since large-scale modes are important to SASI and small-scale turbulence behaves very differently in two dimensions than in three (Kraichnan 1967). In contrast, our octant simulations suppress the large-scale $\ell = 1$ modes but still permit true 3D fluid dynamics at small scales. A comparison of the shock evolutions of s27OH and s27FH suggests that the suppression of large-scale ℓ-modes makes it more challenging for shock runaway to occur, all other things being equal at small scales.

The reasons for more rapid shock runaway at low resolution are less clear. We find the properties of the neutrino field depend minimally on the resolution (see Figure 6). Therefore, the differences are unlikely to be due to spatial resolution dependence of the neutrino transport. Nevertheless, it is possible that differences in the structure of the gain region can result in differences in neutrino heating. The net heating rates and heating efficiencies in the gain regions of the simulations are shown in Figure 7. We define the net heating rate $Q_{\rm net}$ as the integrated net neutrino heating over regions that are experiencing net local heating. The neutrino heating efficiency η is defined as the ratio of the net neutrino heating to the sum of the electron neutrino and electron antineutrino luminosities just below the gain radius. In the first ∼75 ms, there are minimal differences between the four models. As the shock radii of the models begin to diverge, the heating rates also diverge, with models with larger shock radii experiencing higher heating rates and heating efficiencies. The models s27FL and s27OL have similar averaged heating rates, although s27OL experiences larger fluctuations once convection has developed. The average heating rate of s27FH is slightly higher than the heating rate of s27OH, which also has smaller average and maximum shock radii. The neutrino heating rate also

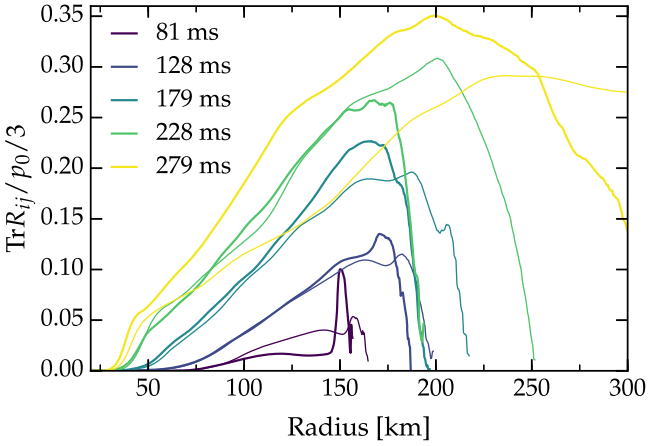

Figure 8. Ratio of the Reynolds pressure (i.e., $\mathrm{Tr}\,R_{ij}/3$) to the the average thermal pressure in the gain region. The ratio as a function of the radius is shown at various times in s27FH (thick lines) and s27FL (thin lines). Comparison with the *rr* component of the Reynolds stress gives similar results, although the maximum of $R_{rr}/p_0 \approx 0.5$.

shows non-radial variations due to non-radial variations in the conditions of the fluid. If the net heating rate is decomposed into spherical harmonics, the time evolution of the different modes is similar to the evolution of the spherical harmonic modes of the shock decomposition. Therefore, it seems likely that the differences between the simulations are due to variations in the hydrodynamics rather than in the neutrino transport.

It is also possible that resolution may affect the properties of turbulence in our simulations. Therefore, we analyze our results in terms of the mean flow equations (e.g., Pope 2000). The Reynolds stress can play a significant role in the momentum equation in the gain region and behind the shock (Murphy & Meakin 2011; Murphy et al. 2013; Handy et al. 2014; Couch & Ott 2015; Radice et al. 2016). We denote the Reynolds stress by $R_{ij} = \langle \rho v_i' v_j' \rangle$, where primes denote fluctuations away from the mean. $\mathrm{Tr}\,R_{ij}/3$ acts like a pressure in the averaged momentum equation, and $\mathrm{Tr}\,R_{ij}/2$ is the kinetic energy contained in velocity fluctuations (Pope 2000). In Figure 8, we show the ratio of the Reynolds pressure to the average thermal pressure found in our simulations. Similar to Couch & Ott (2015) and Radice et al. (2016), we find that the Reynolds pressure can be as high as a third of the thermal pressure in a large portion of the gain region. The maximum contribution of the Reynolds stress is found near the shock front.

From the perspective of the Reynolds-decomposed Navier–Stokes equations, what matters is the total energy contained in turbulent motions. The total energy is directly related to the effective turbulent pressure, which can contribute significantly to the total pressure in the postshock region and aid shock expansion. Abdikamalov et al. (2015) suggested that the resolution dependence of CCSN simulations is due to differences in the spectrum of turbulence with different effective numerical viscosities. However, their Figure 13 shows little resolution dependence on the turbulent kinetic energy at the large energy-containing scales that contributed most to the turbulent pressure. Rather, they found that resolution strongly affects the dissipation range, but the dissipation range contains only a small fraction of the total turbulent kinetic energy at any resolution. This is consistent with the approximately equal Reynolds stresses we see in between in Figure 8.

Since the Reynolds stress contribution to the momentum equation can be a large fraction of the contribution of the thermal pressure, it is instructive to consider the evolution equation of the trace of the Reynolds stress. Including compressibility and buoyancy effects, the trace of the Reynolds transport equation is given by Murphy & Meakin (2011):

$$\partial_t K + \partial_i (v^i K + F_K^i + F_P^i) = \dot{\epsilon}_S + \dot{\epsilon}_B + \langle P' \partial_i v^i \rangle - \rho_0 \epsilon_\nu, \tag{3}$$

where K is the trace of the Reynolds stress, $F_K^i = \langle \rho v_i' v' \cdot v' \rangle$ is the flux due to turbulent transport, $F_P = \langle P' v' \rangle$ is the flux due to pressure fluctuations, and the terms of the right-hand side are the shear production term $\dot{\epsilon}_S = R_{ij} \partial_j v_i$, the buoyancy production term $\dot{\epsilon}_B = \langle \rho' v_i' \rangle g^i$ (g^i is the gravitational acceleration), the work due to turbulent pressure $\langle P' \partial_i v^i \rangle$, and the viscous dissipation $\rho_0 \epsilon_\nu$. The discussion here is mostly qualitative, and we make no attempt to include general-relativistic effects. These effects are small anyway, since the turbulent gain region is far away from the protoneutron star.

In Figure 9, we show the Reynolds stress and the various terms that contribute to its evolution, integrated over the angle, i.e., $4\pi r^2 \langle \rho v^i v_i \rangle$, for s27FH and s27FL. We assume that the average flow is spherically symmetric, and calculate the average $\langle \cdot \rangle$ over the spherical shells. We neglect regions that lie outside of the shock. Although we do not plot it here, we find the well-known result that neutrino-driven turbulence is anisotropic on large scales with $R_{rr} \sim 2R_{\theta\theta} \sim 2R_{\phi\phi}$ (e.g., Murphy et al. 2013; Couch & Ott 2015; Radice et al. 2016). At all times before shock runaway, the Reynolds stress of s27FL tracks the Reynolds stress of s27FH below ~100 km. The bottom panel of Figure 9 shows the net production of Reynolds stress in the gain region. As was suggested by Murphy et al. (2013), buoyancy forces provide the dominant contribution throughout most of the gain region, although, at times, the shear production term can dominate the production just behind the shock, where the average fluid velocity is changing rapidly. The production is qualitatively similar in s27FH and s27FL, but it is systematically higher at large radii in s27FL. Throughout most of the gain region, the Reynolds stress flux is inward and is dominated by the $v^i K$ term. Only near the shock is there a small, outward flux of K. Once again, the high- and low-resolution models are qualitatively similar.

We cannot easily extract the turbulent dissipation rate ϵ_ν from our simulations. Nevertheless, we can infer some of its properties from differences in the Reynolds stress with the resolution. If the dissipation rate were very sensitive to resolution, we would expect the Reynolds stress to saturate at significantly different values when the resolution was changed. Rather, we find that the Reynolds stress does not depend sensitively on resolution once turbulence is fully developed. This result was also seen in the parameterized simulations of Radice et al. (2016), which extended to much higher resolutions than we can consider here.

During the period in which neutrino-driven convection is developing (i.e., before ~100 ms after bounce), s27FL has a Reynolds stress that is a factor of ~2 larger than that of s27FH from 100 to 150 km. This can also be seen in the top row of Figure 1, where the lower-resolution models have convective plumes developing at slightly larger radii than the higher-

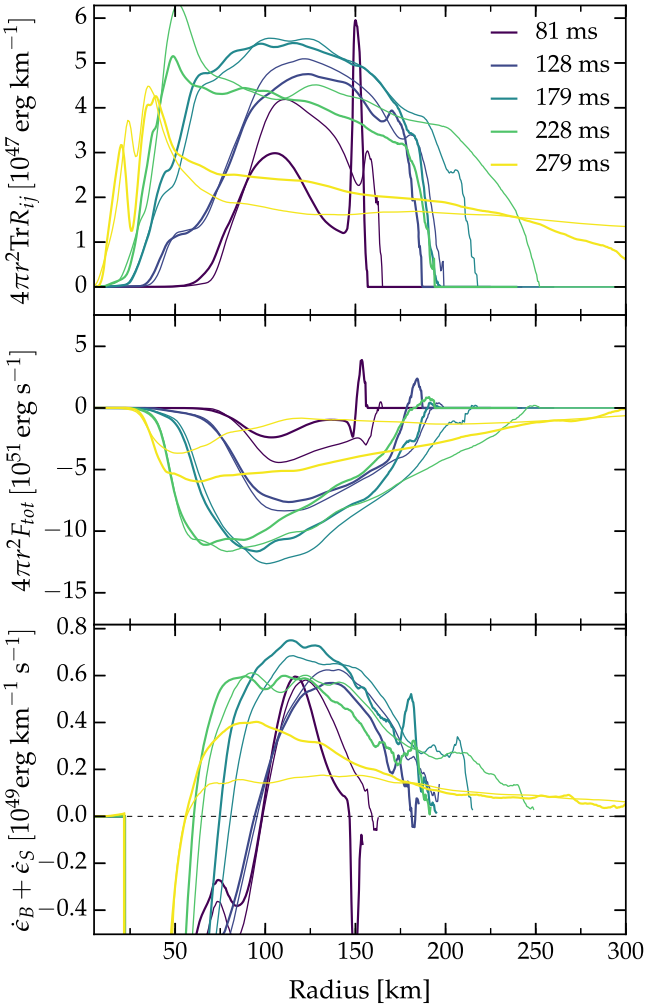

Figure 9. Trace of the Reynolds stress and related quantities vs. the radius at various times in s27FH (thick lines) and s27FL (thin lines). Top Panel: the trace of the Reynolds stress integrated over the angle. Middle Panel: the total flux of the trace of the Reynolds stress. Throughout most of the gain region, the flux is dominated by the average velocity advection term. Near the shock, both pressure fluctuations and turbulent convection significantly contribute. Bottom Panel: the Reynolds production by buoyancy and shear. Buoyancy is the dominant contributor throughout most of the gain region, but the shear term contributes significantly near the shock.

resolution models. This could potentially account for the somewhat more rapid shock expansion seen in s27FL during the first ∼100 ms of evolution, although the extra contribution to the pressure is at most only a few percent. A plausible explanation for this difference is that larger perturbations due to low resolution result in more convective motion in model s27FL at early times (cf. Ott et al. 2013). This may result in conditions more favorable for early-time shock expansion, which is consistent with the more rapid shock expansion seen in the low-resolution models at early times in Figure 3. This in turn results in a somewhat higher neutrino heating rate and a corresponding neutrino heating efficiency, which makes conditions more favorable for eventual shock runaway.

At later times, when convection appears to be fully developed (see Figure 1), the variation of the Reynolds stress with resolution in the gain region becomes smaller. At 130 ms and 180 ms, K is slightly larger in s27FL above 100 km. Comparing this with Figure 3, we see that the relative shock expansion rate is slightly higher in s27FL. At 230 ms, around the time the shock radii of s27FH and s27FL begin to diverge drastically, s27FL has a much higher Reynolds stress throughout most of the gain region. Nonetheless, the difference in the maximum relative contribution to the pressure is only ∼5% (see Figure 8).

Large grid perturbations are not expected in simulations that employ spherical polar coordinates, but potentially large *physical* perturbations are expected from multi-dimensional stellar evolution simulations (e.g., Couch et al. 2015). In the abscence of physical or ad-hoc imposed perturbations, the accretion flow is spherically symmetric and remains so on spherical polar grids that typically induce much smaller numerical perturbations into the flow than a Cartesian grid does. Although lower resolution was used in the work of Hanke et al. (2013), their simulation using the s27 progenitor employed spherical polar coordinates, and their code is known to preserve spherical symmetry. That model did not undergo shock runaway, while our models using the same progenitor do. Our results suggest that this qualitative difference may be in part due to differences induced by the early strong development of convection. Nevertheless, there are many other differences between our simulation and theirs, so we caution against drawing definitive conclusions. The results of Radice et al. (2016) are an important caveat. They carried out parameterized neutrino-driven convection simulations over a large range of resolutions. Despite their use of perturbation-reducing spherical polar coordinates, they found more rapid shock expansion at early times when the resolution was reduced.

5. CONCLUSIONS

We have carried out fully 3D GR multi-group neutrino radiation-hydrodynamics simulations of the postbounce phase of CCSNe. We employ a 27-$M_\odot$ progenitor and follow its postbounce CCSN evolution for 380 ms at the highest resolution to date. We observe the onset of explosion in low-resolution and high-resolution full 3D simulations.

We find that both resolution and imposed large-scale symmetries can have a significant effect on the pre-explosion dynamics of CCSNe. Shock runaway begins in both of our fully 3D models at ∼230 ms after bounce, soon after accretion of the silicon–oxygen shell interface. While both models undergo shock runaway, the lower-resolution model runs away much more rapidly. The large differences between the hydrodynamic evolution of these two models suggest that at the current resolutions, models of CCSNe are far from being converged, consistent with the results found in parameterized studies (Abdikamalov et al. 2015; Radice et al. 2016). The imposition of octant symmetry in the high-resolution model prevents the shock from running away, while at low resolution, octant symmetry has only a modest effect on the gross features of the shock evolution. In contrast to the hydrodynamic evolution, we find there are only small variations in the properties of the neutrino field between simulations. Our results for the shock evolution of the s27 progenitor contrast with those of Hanke et al. (2013) and Tamborra et al. (2014b), who also performed 3D simulations and found similar neutrino emission but did not observe shock runaway.

In the models that experience shock runaway, the shock expansion is asymmetric. When no symmetries are imposed, the shock runaway in both the high- and low-resolution simulations has a strong, growing $\ell = 1$ deformation. In the octant simulation that experiences shock runaway, there is a

strong $\ell = 2$ deformation, which is the lowest-order asymmetry available in octant symmetry. Similar to what was seen in the radiation-hydrodynamics 3D simulations of Lentz et al. (2015), we find that this asymmetry is in part driven by coherent inflows and outflows during shock runaway. The size of these structures is impacted by the resolution.

In previous work (Abdikamalov et al. 2015; Radice et al. 2015, 2016), some of us argued that an inefficient turbulent cascade at low resolution traps kinetic energy at large scales, artificially enabling shock expansion and explosion. While it is true without doubt that kinetic energy at large scales is what leads to shock expansion (e.g., Dolence et al. 2013), the results of our study suggest a more nuanced view on the resolution dependence of the neutrino mechanism. We find some indication that lower-resolution simulations have more turbulent pressure support than higher-resolution simulations. However, this is true only at certain times and not universally throughout the postbounce evolution. What may be equally or more important is how turbulent convection is started: lower-resolution simulations seed turbulent convection with larger numerical perturbations (Ott et al. 2013; Janka et al. 2016). This results in stronger turbulence early on that pushes the shock out further and establishes a larger gain region, setting the stage for a postbounce evolution that is more favorable for shock runaway and explosion. It may thus be that Mazurek's law[13] about the feedback-damping of perturbations applied to complex nonlinear systems is violated after all: In critical cases, explosion or no explosion may depend on the initial conditions from which turbulence grows. This hypothesis clearly needs further scrutiny, but it falls in line with the interpretation of (developing) turbulence as deterministic chaos (Pope 2000).

The work presented in this paper and the conclusions that we draw have important caveats and limitations. Much more future work is necessary to fully understand neutrino-driven CCSNe. The most important limitations of our work are numerical resolution in the hydrodynamic sector and the neglect of inelastic scattering and velocity dependence in the neutrino sector. The latter two may significantly affect the heating rate in the gain region and thereby the shock evolution. Also, we start our simulations from a 1D postbounce configuration of a single 1D progenitor star. Future simulations should be fully 3D for the entire evolution, should consider a range of progenitors ideally coming from 3D presupernova stellar evolution simulations, and should more conclusively explore the resolution dependence of CCSN turbulence.

The authors would like to thank E Abdikamalov, WD Arnett, A Burrows, S Couch, F Foucart, K Kiuchi, J Lattimer, C Meakin, P Mösta, D Radice, Y Sekiguchi, and M Shibata for their discussions. CDO wishes to thank the Yukawa Institute for Theoretical Physics for their hospitality during the completion of this work. Support for LR during this work was provided by NASA through an Einstein Postdoctoral Fellowship grant, PF3-140114, awarded by the *Chandra* X-ray Center, which is operated by the Smithsonian Astrophysical Observatory for NASA under contract NAS8-03060. This research was partially supported by NSF grants AST-1212170, CAREER PHY-1151197, PHY-1404569, AST-1333520, and OCI-0905046; the Sherman Fairchild Foundation; and the International Research Unit of Advanced Future Studies, Kyoto University. Support for EO during this work was provided by NASA through Hubble Fellowship grant #51344.001-A, awarded by the Space Telescope Science Institute, which is operated by the Association of Universities for Research in Astronomy, Inc., for NASA under contract NAS 5-26555. This research was supported in part by the Perimeter Institute for Theoretical Physics. Research at the Perimeter Institute is supported by the Government of Canada through the Department of Innovation, Science, and Economic Development and by the Province of Ontario through the Ministry of Research and Innovation. The simulations were carried out on the NSF XSEDE network (allocation TG-PHY100033) and on NSF/NCSA Blue Waters (PRAC award ACI-1440083). This paper has been assigned Yukawa Institute for Theoretical Physics report number YITP-16-54.

[13] Mazurek's law originated in the context of stellar collapse at Stony Brook University in the 1980s when Ted Mazurek was there. It is now used to generally refer to the strong feedback in a complicated astrophysical situation which dampens the effect of a change in any single parameter or condition (A. Burrows & J. Lattimer 2016, private communication).

REFERENCES

Abdikamalov, E., Ott, C. D., Radice, D., et al. 2015, ApJ, 808, 70
Baumgarte, T. W., & Shapiro, S. L. 2010, Numerical Relativity: Solving Einstein's Equations on the Computer (Cambridge: Cambridge Univ. Press)
Bethe, H. A., & Wilson, J. R. 1985, ApJ, 295, 14
Blondin, J. M., Mezzacappa, A., & DeMarino, C. 2003, ApJ, 584, 971
Bruenn, S. W. 1985, ApJS, 58, 771
Bruenn, S. W., Lentz, E. J., Hix, W. R., et al. 2016, ApJ, 818, 123
Bruenn, S. W., Mezzacappa, A., Hix, W. R., et al. 2013, ApJL, 767, L6
Burrows, A. 2013, RvMP, 85, 245
Burrows, A., Dessart, L., Livne, E., Ott, C. D., & Murphy, J. 2007, ApJ, 664, 416
Burrows, A., Dolence, J. C., & Murphy, J. W. 2012, ApJ, 759, 5
Cardall, C. Y., Endeve, E., & Mezzacappa, A. 2013, PhRvD, 87, 103004
Couch, S. M. 2013, ApJ, 775, 35
Couch, S. M., Chatzopoulos, E., Arnett, W. D., & Timmes, F. X. 2015, ApJL, 808, L21
Couch, S. M., & O'Connor, E. P. 2014, ApJ, 785, 123
Couch, S. M., & Ott, C. D. 2015, ApJ, 799, 5
Dolence, J. C., Burrows, A., Murphy, J. W., & Nordhaus, J. 2013, ApJ, 765, 110
Dolence, J. C., Burrows, A., & Zhang, W. 2015, ApJ, 800, 10
Fischer, T., Whitehouse, S. C., Mezzacappa, A., Thielemann, F.-K., & Liebendörfer, M. 2010, A&A, 517, A80
Foglizzo, T., Scheck, L., & Janka, H.-T. 2006, ApJ, 652, 1436
Foucart, F., O'Connor, E., Roberts, L., et al. 2015, PhRvD, 91, 124021
Handy, T., Plewa, T., & Odrzywołek, A. 2014, ApJ, 783, 125
Hanke, F., Marek, A., Müller, B., & Janka, H.-T. 2012, ApJ, 755, 138
Hanke, F., Müller, B., Wongwathanarat, A., Marek, A., & Janka, H.-T. 2013, ApJ, 770, 66
Hüdepohl, L., Müller, B., Janka, H.-T., Marek, A., & Raffelt, G. G. 2010, PhRvL, 104, 251101
Iwakami, W., Kotake, K., Ohnishi, N., Yamada, S., & Sawada, K. 2008, ApJ, 678, 1207
Janka, H.-T., Melson, T., & Summa, A. 2016, (arXiv:1602.05576)
Just, O., Obergaulinger, M., & Janka, H.-T. 2015, MNRAS, 453, 3386
Kraichnan, R. H. 1967, PhFl, 10, 1417
Kuroda, T., Takiwaki, T., & Kotake, K. 2016, ApJS, 222, 20
Lattimer, J. M., & Swesty, F. D. 1991, NuPhA, 535, 331
Lentz, E. J., Bruenn, S. W., Hix, W. R., et al. 2015, ApJL, 807, L31
Lentz, E. J., Mezzacappa, A., Messer, O. E. B., et al. 2012, ApJ, 747, 73
Liebendörfer, M., Mezzacappa, A., Thielemann, F.-K., et al. 2001, PhRvD, 63, 103004
Löffler, F., Faber, J., Bentivegna, E., et al. 2012, CQGra, 29, 115001
Melson, T., Janka, H.-T., Bollig, R., et al. 2015, ApJL, 808, L42
Minerbo, G. N. 1978, JQSRT, 20, 541
Mösta, P., Mundim, B. C., Faber, J. A., et al. 2014a, CQGra, 31, 015005
Mösta, P., Ott, C. D., Radice, D., et al. 2015, Natur, 528, 376
Mösta, P., Richers, S., Ott, C. D., et al. 2014b, ApJL, 785, L29
Müller, B., & Janka, H.-T. 2014, ApJ, 788, 82
Müller, B., Janka, H.-T., & Heger, A. 2012a, ApJ, 761, 72
Müller, B., Janka, H.-T., & Marek, A. 2012b, ApJ, 756, 84

Murphy, J. W., Dolence, J. C., & Burrows, A. 2013, ApJ, 771, 52
Murphy, J. W., & Meakin, C. 2011, ApJ, 742, 74
Nordhaus, J., Burrows, A., Almgren, A., & Bell, J. 2010, ApJ, 720, 694
O'Connor, E. 2015, ApJS, 219, 24
O'Connor, E., & Couch, S. M. 2015, ApJ, submitted (arXiv:1511.07443)
O'Connor, E., & Ott, C. D. 2010, CQGra, 27, 114103
O'Connor, E., & Ott, C. D. 2011, ApJ, 730, 70
O'Connor, E., & Ott, C. D. 2013, ApJ, 762, 126
Ott, C. D., Abdikamalov, E., Mösta, P., et al. 2013, ApJ, 768, 115
Ott, C. D., Abdikamalov, E., O'Connor, E., et al. 2012, PhRvD, 86, 024026
Pope, S. B. (ed.) 2000, Turbulent Flows (Cambridge: Cambridge Univ. Press), 83
Radice, D., Couch, S. M., & Ott, C. D. 2015, ComAC, 2, 7
Radice, D., Ott, C. D., Abdikamalov, E., et al. 2016, ApJ, 820, 76
Reisswig, C., Haas, R., Ott, C. D., et al. 2013, PhRvD, 87, 064023
Scheck, L., Janka, H.-T., Foglizzo, T., & Kifonidis, K. 2008, A&A, 477, 931
Shibata, M., Kiuchi, K., Sekiguchi, Y., & Suwa, Y. 2011, PThPh, 125, 1255
Skinner, M. A., Burrows, A., & Dolence, J. C. 2015, ApJ, Submitted (arXiv:1512.00113)
Sumiyoshi, K., Takiwaki, T., Matsufuru, H., & Yamada, S. 2015, ApJS, 216, 5
Tamborra, I., Hanke, F., Janka, H.-T., et al. 2014, ApJ, 792, 96
Tamborra, I., Raffelt, G., Hanke, F., Janka, H.-T., & Müller, B. 2014b, PhRvD, 90, 045032
Thorne, K. S. 1981, MNRAS, 194, 439
Turk, M. J., Smith, B. D., Oishi, J. S., et al. 2011, ApJS, 192, 9
Woosley, S. E., Heger, A., & Weaver, T. A. 2002, RvMP, 74, 1015
Yamasaki, T., & Yamada, S. 2007, ApJ, 656, 1019